Title:

Complimentary vertebrate *Wac* models exhibit phenotypes relevant to DeSanto-Shinawi Syndrome

Kang-Han Lee [1,^], April M Stafford [2,^], Maria Pacheco-Vergara [3], Karol Cichewicz [4,5], Cesar P Canales [4,5], Nicolas Seban [4,5], Melissa Corea [4,5], Darlene Rahbarian [4,5], Kelly E. Bonekamp [6], Grant R. Gillie [6], Dariangelly Pacheco-Cruz [2,7], Alyssa M Gill [2], Hye-Eun Hwang[1], Katie L Uhl [2], Tara E Jager [8], Marwan Shinawi [9], Xiaopeng Li [2], Andre Obenaus [10], Shane Crandall [6,7], Juhee Jeong [3], Alex Nord [4,5], Cheol-Hee Kim [1,#], Daniel Vogt [2,7,#].

Affiliations:

1) Department of Biology, Chungnam National University, Daejeon 34134, Korea
2) Department of Pediatrics and Human Development, College of Human Medicine, Michigan State University, Grand Rapids, MI, 49503, USA.
3) Department of Molecular Pathology, New York University College of Dentistry, New York, NY 10010, USA.
4) Department of Psychiatry and Behavioral Sciences, University of California Davis, Davis 95618, USA.
5) Department of Neurobiology, Physiology and Behavior, University of California Davis, Davis 95618, USA.
6) Department of Physiology, Michigan State University, East Lansing, MI 48824, USA.
7) Neuroscience Program, Michigan State University, East Lansing, MI 48824, USA.
8) Corewell Health, Grand Rapids, MI, 49503, USA.
9) Division of Genetics and Genomic Medicine, Department of Pediatrics, Washington University School of Medicine, St. Louis, MO, 63110, USA.
10) Director, Preclinical and Translational Imaging Center, School of Medicine, University of California Irvine, Irvine, CA 92697, USA.

^ Equal contribution
# Correspondence

Cheol-Hee Kim: zebrakim@cnu.ac.kr
Daniel Vogt: vogtdan2@msu.edu

Abstract
Monogenic syndromes are associated with neurodevelopmental changes that result in cognitive impairments, neurobehavioral phenotypes including autism and attention deficit hyperactivity disorder (ADHD), and seizures. Limited studies and resources are available to make meaningful headway into the underlying molecular mechanisms that result in these symptoms. One such example is DeSanto-Shinawi Syndrome (DESSH), a rare disorder caused by pathogenic variants in the *WAC* gene. Individuals with DESSH syndrome exhibit a recognizable craniofacial gestalt, developmental delay/intellectual disability, neurobehavioral symptoms that include autism, ADHD, behavioral difficulties and seizures. However, no thorough studies from a vertebrate model exist to understand how these changes occur. To overcome this, we developed both murine and zebrafish *Wac/wac* deletion mutants and studied whether their phenotypes recapitulate those described in individuals with DESSH syndrome. We show that the two *Wac* models exhibit craniofacial and behavioral changes, reminiscent of abnormalities found in DESSH syndrome. In addition, each model revealed impacts to GABAergic neurons and further studies showed that the mouse mutants are susceptible to seizures, changes in brain volumes that are different between sexes and relevant behaviors. Finally, we uncovered transcriptional impacts of *Wac* loss of function that will pave the way for future molecular studies into DESSH. These studies begin to uncover some biological underpinnings of DESSH syndrome and elucidate the biology of *Wac*, with advantages in each model.

Introduction
Pathogenic variants in the WW domain-containing adaptor with coiled coil, *Wac*, gene cause a neurodevelopmental (NDD) disorder called DeSanto-Shinawi (DESSH) syndrome (aka WAC-related disorder) [1]. DESSH syndrome is characterized by a constellation of developmental delay/intellectual disability, cranio-facial dysmorphism, hypotonia, seizure, gastrointestinal problems (e.g., constipation and gastroesophageal reflux), and ophthalmological abnormalities (e.g., refractive errors and strabismus) [1]. In addition, individuals with DESSH syndrome exhibit arrays of neurobehavioral phenotypes including aggression, attention deficit hyperactivity disorder (ADHD), autism spectrum disorder (ASD) and anxiety [1–5]. *Wac* is a known autism risk gene due to the enrichment of pathogenic genetic variants in ASD cohorts [6]. However, little is known about the function of WAC in the brain and whether suitable vertebrate models could explore the underlying biology of DESSH syndrome phenotypes.

The *Wac* gene encodes a protein with WW and coiled-coil domains, which are predicted to be important for protein/protein interactions. A multitude of cellular roles for the WAC protein exist, including regulation of mammalian target of rapamycin (mTOR), mitosis, transcription and autophagy [7–10], likely through distinct protein/protein interactions of WAC in different cells and cellular compartments. A recent study assessed the role of various protein domains in the human WAC protein and isolated an amino terminal nuclear localization signal as well as a highly conserved disorganized region that contains several putative phosphorylation motifs that are mutated in humans with known *Wac* variants [11]. The functional role of these domains and of WAC itself are still poorly understood in vertebrates. While previous studies in drosophila and immortalized cell lines suggested cellular and nuclear functions for WAC, what relevant symptoms may occur in vertebrates is unknown.

We generated two species-specific vertebrate deletion models to assess whether *Wac* depletion could recapitulate symptoms associated with DESSH syndrome. The rationale for choosing mouse and zebrafish models were: 1) Both are vertebrates; 2) Unique genetic approaches in each model; 3) Species-specific phenotypic screening advantages; 4) Finally, utilizing two distinct vertebrate models to study key brain phenotypes will be a powerful means to uncover the fundamental biology of DESSH syndrome in a manner that is likely to reveal novel neurological underpinnings.

Our models revealed key similarities and features that could be advantageous. Mouse constitutive knockout (KO)s were not viable but heterozygous progeny survived. Loss of one of the *wac* isoforms led to phenotypes in zebrafish, consistent with the mouse model. Mutants exhibited core phenotypes observed in those diagnosed with DESSH syndrome, including dysmorphic craniofacial features, susceptibility to seizures, and behaviors implicating decreased learning and social interaction. Both models displayed decreased GABAergic markers, which may underlie some of the symptoms, including seizures. Moreover, our mouse model revealed important changes in brain volume that impacts males more severely and provide the first dataset of RNA changes in the brain that may underlie mechanisms that lead to symptoms relevant to DESSH syndrome behaviors. Our data suggest that these models are a resource for experiments to investigate the efficacy and utility of therapeutic

interventions for DESSH syndrome and further exploration of the underlying biological mechanisms of this condition.

Results

Validation of murine *Wac* and zebrafish *wac* mutants

We obtained sperm from the International Mouse Phenotyping Consortium (IMPC); the *Wac* murine locus on chromosome 18 was genetically modified to include flanking *loxP* (Flox) sites of exon 5 (Schema, Figure 1a). *Wac flox* founders were bred and crossed to *beta-actin-Cre* mice, which express *Cre* in germ cells [12]. After *Cre* recombination of the locus, some of the intron after exon 4 is translated which contains a stop codon Figure 1b). We generated wild type (WT) and constitutive heterozygous (Het) progeny of similar size (Figure 1c) but not any live homozygous knockouts. The results of genotyping using PCR are shown in Figure 1d. and Sanger-sequencing of the genotyped PCR validated recombination of the locus (data not shown). Findings were consistent with data from the IMPC; constitutive *Wac* KOs are embryonic lethal.

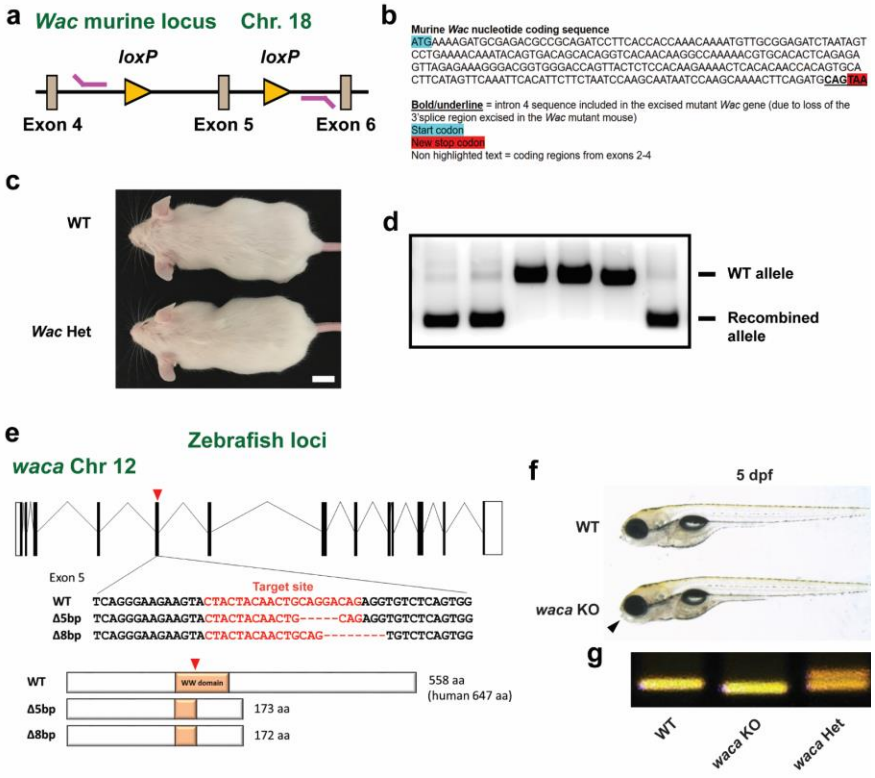

Figure 1: Generation and validation of murine *Wac* and zebrafish *wac* mutants. (a) Floxed mouse *Wac* genetic locus and genotyping primers. Genotyping primers (magenta lines) reside external to the *loxP* sites (orange triangles) flanking exon 5 and nearby introns. (b) Example images of adult WT and *Wac* Het mice. (c) DNA gel of genotyping for WT and recombined (Het) *Wac* alleles. (d) The recombined DNA band was Sanger-sequenced and contains a single recombined *loxP* site (orange) flanked by intronic DNA sequences (magenta and brown text); additional text matches the parent DNA vector used to generate the locus. (e) *waca* KO zebrafish were generated by CRISPR/Cas9. KO target sites for sgRNAs are indicated by red arrowheads and predicted protein structures for KO mutations indicated below panel. (f) WT and *waca* KO zebrafish have grossly normal sizes but *waca* KO exhibited a shortened jaw (black triangle) morphological phenotype at 5 dpf. Abbreviations: (aa) amino acid; (bp) base pair; (Chr) chromosome; (dpf) days post fertilization; (WT) wild type. Scale bars (b) = 1 cm and (f) = 200 µm.

Zebrafish harbor two *wac* loci on chromosome 12, *waca*, and 2, *wacb,* genes. A CRISPR/CAS9 approach was used to target these loci. The *waca* mutant had a deletion in coding exon five (Figure 1e) with *waca* progeny grossly normal in size by 5 days post fertilization (dpf) (Figure 1f). The genotyping results are shown in Figure 1g. The *wacb* mutants had a deletion in exon 3 (Supplementary Figure 1a), but unlike *waca* knockouts (KOs) had a normal appearance (Supplementary Figure 1b); the genotyping results of *wacb* are shown in Supplementary Figure 1c. While the *wacb* KOs exhibited no overt phenotypes so far, the *waca* KOs were phenotypic with shorten lower jaw (Figure 1f) and broad nasal tip (Supplementary Figure 1d) and we chose to focus our main zebrafish analyses on this genotype. We generated *waca* and *wacb* double genes KO (dKO) to confirm whether early lethal occurs in the zebrafish as well. The *wac* dKO zebrafish showed small head, heart edema, shorten jaw and failure of swim bladder inflation, suggesting early lethal phenotype like *Wac* KO mice (Supplementary Figure 1e). Finally, we sought to validate loss of *waca* and *wacb* RNA in the single and dKO brains, however, we found that *waca* transcript was elevated, suggesting that this may be compensatory reaction to the mutation. We could not validate the zebrafish protein level but later we provide evidence that a compensatory increase in *Wac* RNA also occurs in mouse but is not made into protein.

Craniofacial changes in murine and zebrafish mutants

Craniofacial dysmorphism is a cardinal feature in patients with DESSH syndrome [1–3, 5, 13–17]. We wondered whether a reduction in *Wac* dosage in mice can recapitulate this finding. Postnatal day (P)0 and P30 mouse skulls were examined. During neonatal ages, a widening of the fontanels and sutures along the midline of the

calvaria was noted (Figure 2a, 2b). While both the anterior and posterior regions of the calvaria were affected, the anterior region had the greater change (Figure 2a, 2b, 2e, 2f with pseudo-colored areas in 2a', 2b'; anterior p = 0.0001, posterior p = 0.01). By P30, there remained a noticeable gap in the interfrontal suture of *Wac* Het. Concomitantly, the width of the skull across the frontal bones was significantly increased in *Wac* Hets, while the width across the parietal bones was not altered (Figure 2c, 2d, 2g, 2h, p = 0.002 Frontal width). We noted gross changes in *waca* zebrafish mutants in Figure 1, so we investigated further, A feature that was notable was a shortened lower jaw in the *waca* KO zebrafish compared to WTs at 10 dpf (Figure 2i-k, p = 0.006). In addition, the *waca* mutants also exhibited changes in other craniofacial features, including an increased width spanning Meckel's cartilage at 13 dpf (Figure 2l-n, p = 0.02). The *waca* KO zebrafish survived to adulthood and showed morphological craniofacial defects of shortened lower jaw, sunken head and broad nasal tip at adult stage (Supplementary Figure 1f-h'). Thus, both models exhibit craniofacial changes relevant to DESSH syndrome.

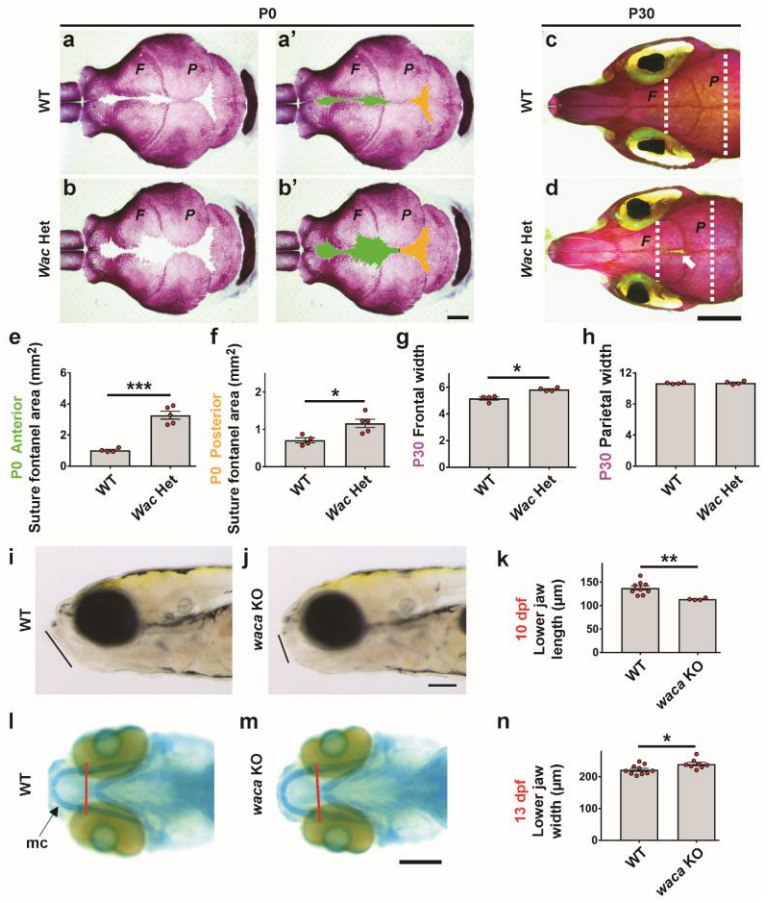

Figure 2: Craniofacial changes in mutants. (a, b) Dorsal views of the P0 calvaria stained with Alizarin red for bone. (a', b') The suture and fontanel areas in (a) and (b) are pseudo-colored green (anterior) and orange (posterior). (c, d) Dorsal views of P30 WT and *Wac* Het skull bones; arrow (d) points to a gap in the interfrontal suture. (*F*) Frontal bone and (*P*) Parietal bone; white dashed lines are widths measured in (g, h). (e, f) Quantification of P0 fontanel suture areas pseudo colored in a' and b'; WT n = 4, Het n = 5. Quantification of the skull width across the frontal (g) and parietal (h) bones at P30 in WTs and *Wac* Hets; WT n = 4, Het n = 4. (I, j) The *waca* KO zebrafish show a shortened jaw structure, compared to WT. Lines denote lower jaw length. (k) Quantification of lower jaw length, data expressed as the mean ± SEM; n = 9 WT, 11 *waca* Het and 4 *waca* KO, **p < 0.01. (l, m) Cartilage staining of zebrafish using alcian blue, ventral view. (n) Measurements of the width of Meckel's cartilage in *waca* KO zebrafish at 13 dpf (red line); WT n=10, KO n = 8. Data are expressed as the mean ± SEM. *p < 0.05 and ***p < 0.001. Scale bars (b') = 1 mm, (d) = 4 mm, (j, m) = 200 µm.

Behavioral changes in *Wac/wac* mutants

Loss of *Wac* may impact social/cognitive behavior, as seen among individuals diagnosed with DESSH syndrome and models exhibit intellectual challenges [3, 5, 14, 15, 17]. Het mutant mice had normal ambulation (Supplementary Figure 2a). While they spent more time with a novel mouse, *Wac* Hets showed less distinction between a mouse and object, while WTs showed significant differences (Figure 3a, p = 0.005). *Wac* Hets also had significant impairments in the Y-maze that tests working memory [18, 19] (Figure 3b, p = 0.047). Anxiety and spatial memory were not grossly changed but cohorts of *Wac* Hets trended towards impairment in each test (Supplementary Figure 2b, 2c). We did not find any differences between males and females in behavior.

When male zebrafish were tested in a social cohesion assay, WT fish stayed in close contact while *waca* KOs were dispersed during the trial (Figure 3c-3e, p = 0.0007). In a novel tank assay, male *waca* KO fish moved greater distances, indicating hyperactivity, throughout the test compared to WTs (Figure 3f, 3g, p = 0.005). Despite showing the same social cohesion deficits, female *waca* KOs did not show the same tendency to travel greater distances (Supplementary Figure 3c). However, female *waca* KOs showed greater swimming duration time in C zone and decrease of duration time in A zone, indicating anxiolytic behavior in the novel tank assay (Supplementary Figure 3a-3b', 3d-3e p<0.0001); males did not show differences (Supplementary Figure 3f, 3g). The *wacb* KOs showed normal social cohesion and locomotion (Supplementary Figure 4a-4g). The *waca* KOs were also assessed for aggression and reaction to an alarm stimulus. They showed normal responses in each test, however, in the aggression mirror biting test, they moved greater distances in the tank compared to WTs

(Supplementary Figure 5a-5f, $p < 0.0001$). While some differences exist in locomotion, both models share deficits in social interaction.

Increased murine brain volume in multiple regions with a male bias

To determine what regions of the mutant brains may be anatomically different, we used our mouse model to perform magnetic resonance imaging (MRI) on P30 fixed WT and *Wac* Het brains of both sexes. We first assessed total brain volume of the WT and mutant brains and found that male *Wac* mutants exhibit a larger whole brain volume than WT males; there were no differences in female brain volumes (Figure 4, $p = 0.04$). Next, we examined specific regional volumetric changes, starting with cortical domains. Several alterations were observed in both males and some in females, with most cortical regions showing an increase in volume compared to WTs (Figure 5). Notably, only males had increased retrosplenial cortices, while females showed increases in parietal cortices (Figure 5a, 5b, retrosplenial cortex male Het vs male WT $p = 0.002$ and female WT vs. female Het $p = 0.01$).

We also examined limbic regions and white matter track volumes in WTs and *Wac* Hets. As before, male mice often had significant increases in both limbic and white matter volumes compared to females. Specifically, hippocampal ventral CA3 and dorsal CA1 regions were increased in males but not females (Supplementary Figure 6a, 6b, ventral CA3 male WT vs. male Het $p = 0.0003$ and dorsal CA1 male WT vs. male Het $p = 0.04$). Male specific increased volume was also observed in white matter dorsal fornix and corpus callosum tracts (Supplementary Figure 7a, 7b, dorsal fornix male WT vs. male Het $p = 0.006$ and corpus callosum male WT vs. male Het $p = 0.01$). Unfortunately, few diagnosed DESSH syndrome individuals are adults and MRI data for the younger populations have not been acquired to date. However, these observations may be a potential predictor of phenotypes that may arise as those with DESSH syndrome age into adulthood and whether there could be sex differences in humans.

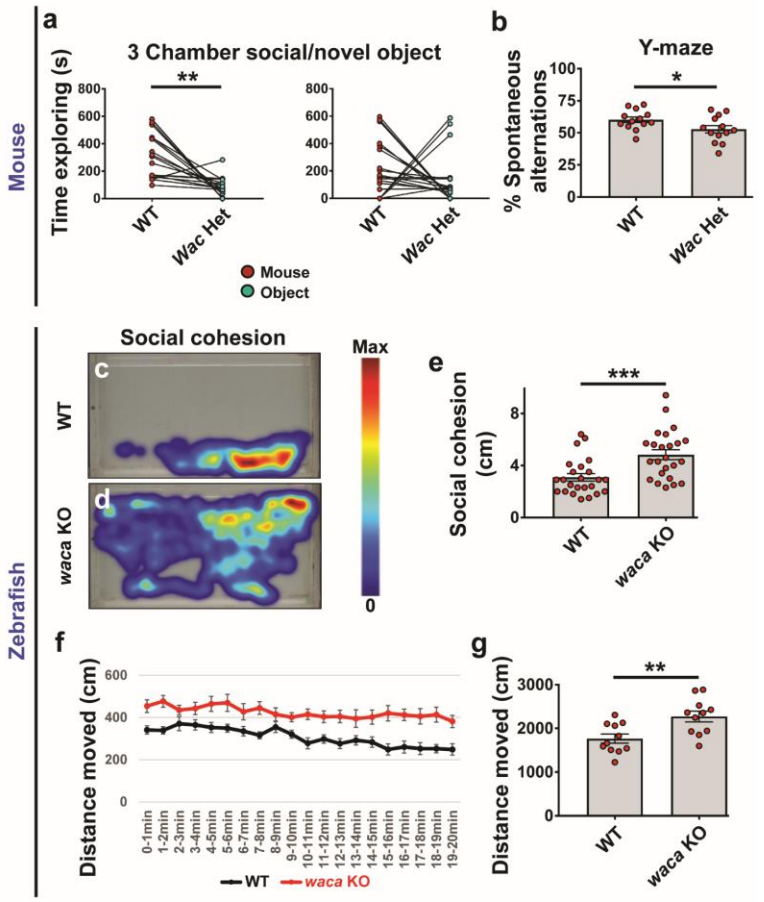

Figure 3: Behavioral changes in mutants. (a) 6-8 week WT and *Wac* Het mice were tested in the 3-chamber social/novel object test, WT n = 16 and Het n = 15, and the Y-maze (b), n = 13 both groups, with *Wac* Hets showing deficits in each. (c, d) Example heat maps during the 17-19 minute timeframe of the social cohesion test in zebrafish; *waca* KOs were more dispersed (e), n = 10 fish per group, 24 screenshot analyzed for (e). (f, g) Distance moved was greater in the *waca* KOs in the novel tank assay, n = 11, both groups. Data are expressed as the mean ± SEM; *p < 0.05, **p < 0.01 and ***p < 0.001.

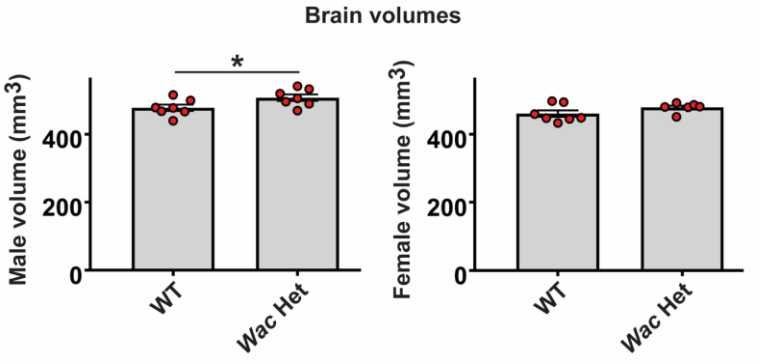

Figure 4: MRI reveals increased brain volume in mouse *Wac* Het males. There was a significant increase in whole brain volumes in HET compared to WT male mice. Female HET mice did not exhibit significant changes in brain volume relative to WT. Data are expressed as the mean ± SEM; *p < 0.05.

Normal numbers of major brain cell types and proteins in murine *Wac* mutant brains

To determine if any major cell types of the brain were altered by loss of *Wac*, we probed for different classes of neurons, as well as oligodendrocytes, astrocytes and microglia in P30 somatosensory

cortices (Figure 6a and Supplementary Figure 8a-8d, 8a'-8d'). The total number of neurons were assessed by labeling for NeuN, while oligodendrocytes, astrocytes and microglia were labeled with OLIG2, S100beta and IBA1, respectively. No differences in these major cell types were observed between the genotypes in mice.

We also assessed mouse P30 somatosensory cortices for proteins changed in other *Wac* models or markers of brain circuits. As expected, WAC protein was reduced 64% in the Hets (Figure 6b, 6c, p = 0.002). Despite previous reports in other models [7, 9], we did not observe differences in mTOR activity or ubiquitination of histone 2B. Key pathways including Wnt/beta-catenin and synaptic markers, PSD95 (excitatory synapses) and Gephyrin/Gad65/67 (inhibitory synapses), were not altered (Figure 6b, 6c). There was a decrease in active ERK1, 38% and ERK2, 33%, in the *Wac* Hets (Figure 6b, 6c, ERK1 p = 0.01, ERK2 p = 0.02), suggesting that while major cell types and proteins involved brain function are not altered, some signaling events may be candidates for future studies to understand WAC function.

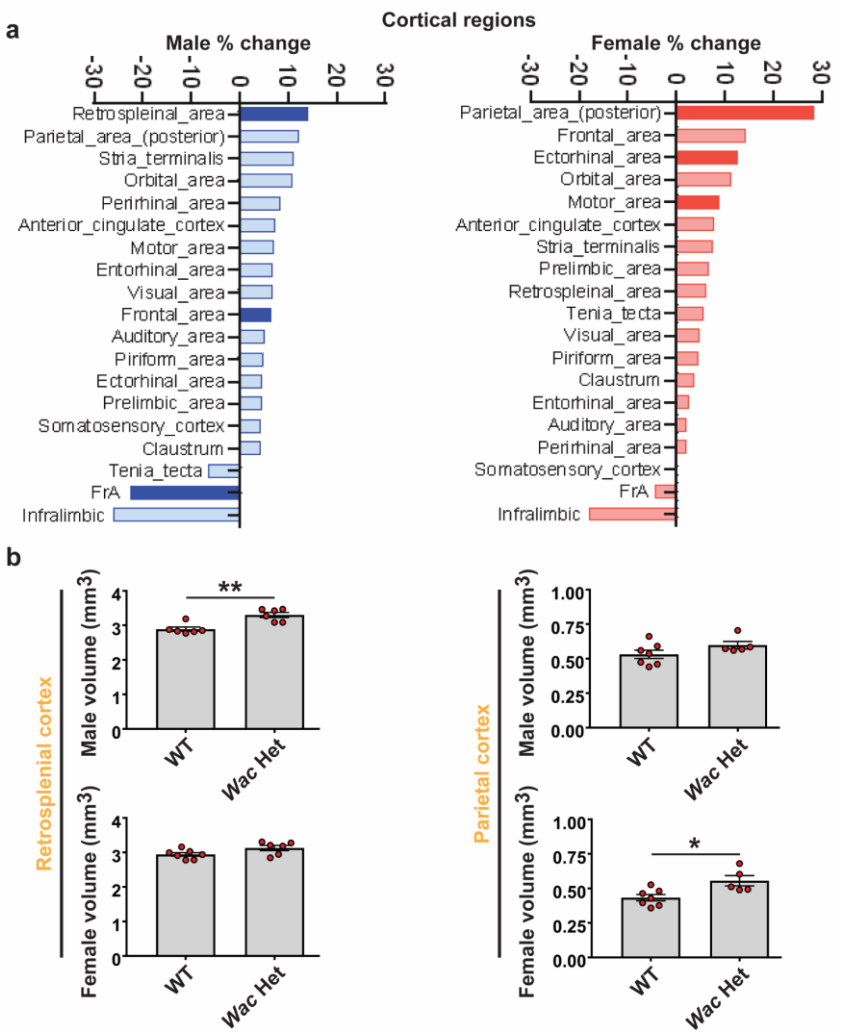

Figure 5: Volumetric regional change in cortical areas. (a) Percent change between cortical regions were larger in HET mice than WT apart from frontal association area (FrA) and infralimbic prefrontal cortex. Similar regions changes were seen in both males and females, although females showed larger changes. (Bolded bars indicate significant differences p<0.05, t-test). (b) Retrosplenial cortex was significantly increased in male HET mice compared to WT but not in female mice. In contrast, while elevated in males, female HET mice exhibited increased parietal cortical volumes compared to WT mice. Data are expressed as the mean ± SEM; *p < 0.05 and **p < 0.01.

Normal pyramidal neuron lamination and electrophysiological properties in murine *Wac* Hets

We assessed glutamatergic neuron laminar markers in the somatosensory cortices of P30 mice. SATB2, CTIP2 and TBR1 were labeled and the proportion of expressing neurons assessed in layers 2/3/4, 5 and 6, however, there were no significant laminar changes in the Het (Supplementary Figure 9a-9i). To further assess if glutamatergic pyramidal neurons were impacted by depletion of *Wac*, we examined the intrinsic membrane properties of layer 2/3 neurons in the primary somatosensory cortex of P46-55 mice. Overall, there were no gross differences in passive or active membrane properties between *Wac* Het and WT cells (Supplementary Figure 9j, 9k and Supplementary Table 1), suggesting excitatory cortical neurons in the mutants have normal physiological properties. We also assessed synaptic function by measuring spontaneous excitatory postsynaptic currents (EPSCs) in layer 2/3 neurons. We found no differences between WT and *Wac* Het excitatory neurons (Supplementary Figure 9l, 9m), further suggesting that the local excitatory circuit in the cortex is not measurably impacted by *Wac* depletion. Thus, we next probed inhibitory GABAergic cortical inhibitory interneurons for any alterations.

Some GABAergic deficits in mouse and zebrafish *Wac/wac* mutants

GABAergic cortical interneurons (CINs), a diverse group of inhibitory neurons whose dysfunction has been implicated in other syndromes [20–25], are highly diverse. To assess whether *Wac* may impact CINs, we assessed 3 broad groups of CINs; parvalbumin (PV)+ and somatostatin (SST)+, which label ~70% of GABAergic

interneurons [26], and prospero homeobox 1 (PROX1) expressing, which labels the majority of caudal derived interneurons [27]. The cell density of SST and PROX1 CINs were normal, but there was ~18% decrease in PV+ CINs in the Het (Figure 7a-7d, p = 0.02). To probe whether PV expression is due to loss of cells or simply the expression of PV, we assessed for the CIN marker, LHX6, which is expressed in all PV+ CINs in the somatosensory cortex [25]. We found no decrease in LHX6 cell numbers (Figure 7a, 7e-7g), suggesting this phenotype is likely due to a change in PV expression rather than loss of this group of interneurons.

We also studied GABAergic markers in *waca* KO zebrafish. While global patterns of *gad1b* expression seemed to be not grossly changed, there was a *gad1b* reduction in *wac* dKO forebrain regions that lacked both *waca* and *wacb* (Figure 7h-7l, dKO vs. WT p = 0.0007, vs. *waca* p = 0.002 and *wacb* p = <0.0001), suggesting a common impairment on GABAergic systems between the two model systems. Since *waca* mutants were trending towards less *gad1b* expression, we wanted to further examine whether *waca* mutants might have reduced expression in this forebrain region. Thus, we compared *gad1b* expression in WTs and *waca* KOs and found a significant reduction in expression (Figure 7m-7q, p<0.0001). These and previous data suggest that GABAergic circuits are a likely culprit underlying symptoms in DESSH syndrome.

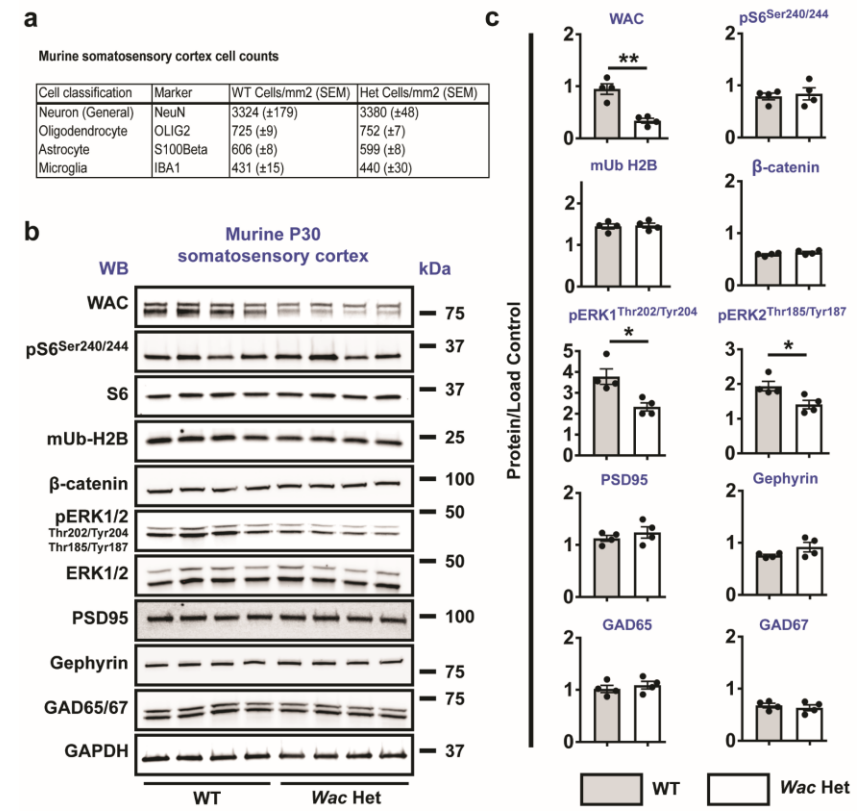

Cell classification	Marker	WT Cells/mm2 (SEM)	Het Cells/mm2 (SEM)
Neuron (General)	NeuN	3324 (±179)	3380 (±48)
Oligodendrocyte	OLIG2	725 (±9)	752 (±7)
Astrocyte	S100Beta	606 (±8)	599 (±8)
Microglia	IBA1	431 (±15)	440 (±30)

Figure 6: Cell counts and biochemical assessment of key markers in P30 *Wac* WT and Het mice. (a) WT and *Wac* Het somatosensory cortices were counted for major cell classes, including markers of neurons and glia, n = 3 each group. (b) P30 somatosensory cortex tissue was probed via western blotting for WAC and proteins known to be altered in other models or of brain groups. (c) Quantification of protein bands were normalized to GAPDH or the total protein if a phosphorylated protein. Data are expressed as the mean ± SEM, n = 4 both groups. * p < 0.05 and ** p < 0.01. Abbreviations: (WB) western blot and (kDa) kiloDaltons.

Elevated seizure susceptibility in *Wac* heterozygous mice

Since inhibitory GABAergic cells were impacted and epilepsy has been observed in individuals with DESSH syndrome [1, 3, 4, 15, 17], we tested if constitutive loss of one *Wac* allele was sufficient to increase seizures in our mouse model. Thus, the GABAA receptor antagonist, pentylenetetrazol (PTZ), was administered intraperitoneal at a subthreshold dose (50mg PTZ per kilogram of mouse body weight) that rarely elicited a tonic-clonic seizure in WTs. We hypothesized that if loss of *Wac* promoted a shift favoring brain excitation/inhibition then *Wac* hets would exhibit more severe seizure behaviors by P30.

PTZ was administered and mice were observed for 20 minutes (Schema, Figure 8a); most mice fully recovered by 15 minutes and all WT mice did not exhibit any behavioral changes by twenty minutes post injection. Behaviors included freezing, motor twitches, loss of balance, seizures and hyperactivity, which are detailed in the methods. We found no sex differences in the ability of PTZ to elicit seizures in WT mice. PTZ led to subtle behavioral changes in both female and male WT mice but rarely elicited a seizure (Figure 8b and 8c). However, both sexes of *Wac* hets exhibited elevated seizure behaviors, including hunched body posture, arching tail and forelimb clonus as well as succumbing to seizures (Figure 8b and 8c; females p = 0.0008 and males p = 0.0047). Thus, loss of *Wac* leads to increased seizure susceptibility in mice, consistent with one of the comorbidities observed in 40-50% of individuals with DESSH syndrome.

RNA sequencing of mouse forebrains reveals DESSH syndrome candidate transcripts

To discover potential molecular changes that could inform future mechanistic studies, we performed bulk RNA-seq at P2, an age when mice are undergoing critical developmental milestones, including neuronal migration, cell death, axon and dendrite outgrowth as well as beginning synaptogenesis. We sequenced 14 WT and 10 *Wac* Het sex-balanced forebrain samples (Supplementary Table 2), to a median sequencing depth of 50 million paired-end reads per sample (Supplementary Figure 10a; Supplementary Table 2). As expected, we found significant correlations between sample sex and sequencing depth, and principal component analysis (PCA) dimensions. No outliers were detected in the PCA space (Supplementary Figure 11a-11c).

Differential expression (DE) analysis was performed using edgeR general linear model (GLM), complemented with SVA batch correction method [28]. Due to reduced sample size, sex-stratified DE was performed without model corrections. At FDR < 0.1, 7 and 16 genes were significantly upregulated and downregulated, respectively; and 385 and 564 upregulated and downregulated genes at a more inclusive P < 0.05 threshold. The directionality of DE was skewed towards downregulation, which is consistent with *Wac* function in promoting transcription [7] (Figure 9a, 9b, Supplementary Tables 3-5). While *Wac* gene expression was subtly upregulated in the mutants (log2FC = 0.09, P = 0.01, FDR = 0.5), coverage of *floxed Wac* exon 5 was reduced by 50% in Het samples (Supplementary Figure 12a, 12b), consistent with compensatory upregulation. Western blot found decreased WAC protein expression (Figure 6) and no evidence of mutant isoforms, demonstrating that mutant *Wac* transcript is unlikely to be stably translated.

Sex-stratified DE in females identified 3 genes passing FDR < 0.1, 1 upregulated and 2 downregulated, and 0 DE genes in males. At P < 0.05, the number of DE genes was higher in males, with 303 upregulated and 275 downregulated, in contrast to 193 upregulated and 149 downregulated genes in females (Figure 9a). Sex-stratified transcriptomic signatures were

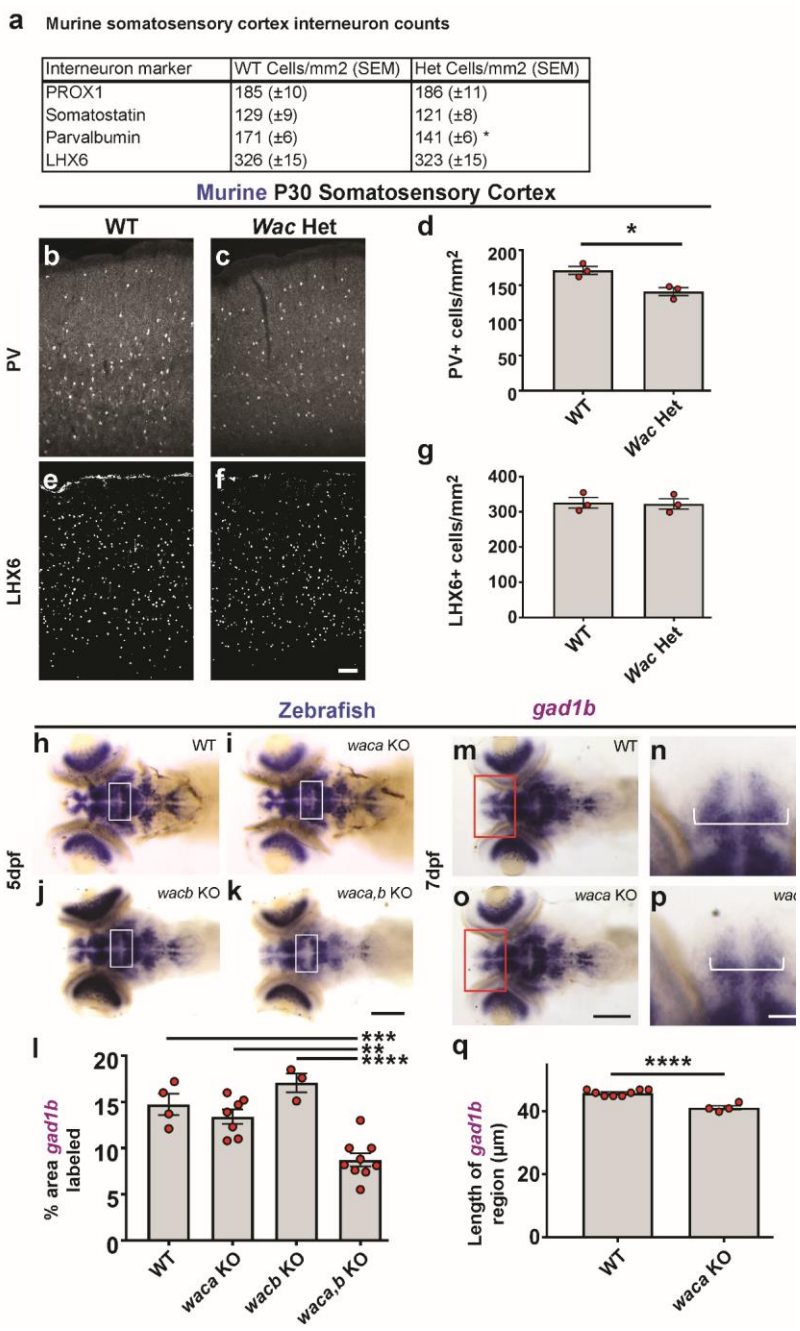

Interneuron marker	WT Cells/mm2 (SEM)	Het Cells/mm2 (SEM)
PROX1	185 (±10)	186 (±11)
Somatostatin	129 (±9)	121 (±8)
Parvalbumin	171 (±6)	141 (±6) *
LHX6	326 (±15)	323 (±15)

Figure 7: Mouse and zebrafish mutants exhibit decreased GABAergic markers. (a) Table of cortical interneuron cell counts in the somatosensory cortex at P30. (b-d) Immunofluorescent images of PV and cell density quantification in mice somatosensory cortex, n = 3, both groups. (e-g) Immunofluorescent images of LHX6 and cell density quantification in mice somatosensory cortex, n = 3, both groups. Zebrafish *gad1b* mRNA expression was examined by whole-mount *in situ* hybridization. (h-k) Dorsal view at 5 dpf, anterior is to the left. *gad1b* expression was qualitatively decreased in *wac* dKO (marked with white box in the midbrain-hindbrain region), compared to WT, *waca KO, and wacb* KO. n = 4 for WT, n = 7 for *waca* KO, n = 3 for *wacb* KO, and n = 9 for *waca*,*b* dKO. (l, n) At 7 dpf, a reduction of *gad1b* was also observed in the forebrain region of *waca* KO zebrafish. (m, o) Magnification of forebrain region boxed in (l, n), anterior is to the top. (p) Measurement of *gad1b*-positive population in the forebrain marked in (m, o). Data are expressed as the mean ± SEM, *p < 0.05, n = 8 for WT, n = 19 for Het, and n = 4 for KO. Scale bars = 100µm (f), 200 µm (k, o), 50 µm (p).

directionally correlated with each other, indicating similarity and consistency of the signatures across sexes and replicates. (Supplementary Figure 13a). However, the higher number of genes passing P < 0.05 in males suggests a potential sex-bias of differential expression (Figure 9a), potentially similar to the greater changes in mouse MRI brain volumes in males.

Gene ontology enrichment analysis of 23 genes passing FDR < 0.1 (Figure 9b, 9c, Supplementary Figure 14) identified significant enrichment of three biological processes: 1) cell adhesion, GO:0007155; 2) positive regulation of neuron differentiation, GO:0045666, and 3) regulation of cytokine production, GO:0001817 (Figure 9d, Supplementary Table 6). B-cell lymphoma 6 (*Bcl6*), downregulated in *Wac* Het, represents a shared gene across all three enriched ontologies. *Bcl6* is a zinc finger transcription factor, which acts as a sequence-specific repressor of transcription, known for its role as a lineage-defining factor of follicular helper T cells [29]. During corticogenesis, *Bcl6* acts as a driver of neurogenesis, promoting the transition from self-renewing neuronal progenitor cells to postmitotic neurons [30], and granule neuron precursors to granule cells in the cerebellum [31]. *Bcl6* has also been demonstrated to promote survival of cortical projection neurons in the early postnatal brain [32] (Figure 9e).

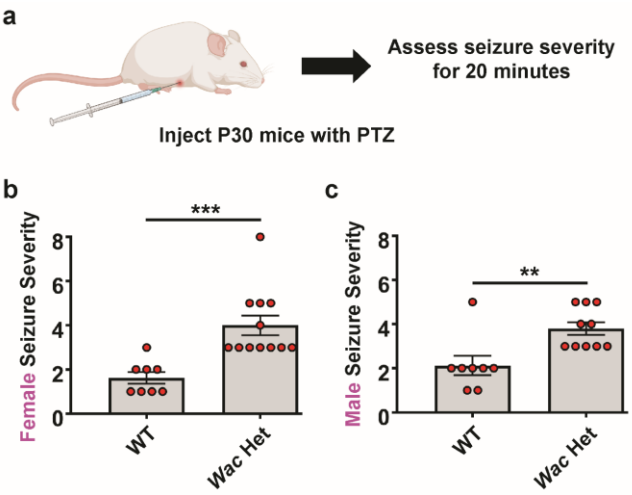

Figure 8: *Wac* depletion leads to elevated seizure susceptibility. (a) Schema depicting the seizure induction by PTZ. Briefly, P30 mice were administered PTZ intraperitoneally and then assessed for the highest seizure severity score over the course of 20 minutes. The maximum seizure severity score over 20 minutes in females (b) and males (c) demonstrate an increased sensitivity to seizures in the *Wac* Hets. Data are expressed as the mean ± SEM; seizures for females, n = 8 (WT), n = 12 (Het) and for males, n = 8 (WT), n = 10 (Het) biological replicates. **p < 0.01 and ***p < 0.001. Scale bar in (f) = 100 µm.

Upregulation of four protocadherin alpha genes at FDR < 0.1; *Pcdhgα11*, *Pcdhgα6*, *Pcdhgα9* and *Pcdhg8* (Figure 9c, 9e); and additional upregulation of three and downregulation of eight protocadherins at P < 0.05 (Supplemental Table 3) is a prominent phenotype of our *Wac* model. Protocadherins are cell surface proteins, mediating diverse functions in axonal and dendrite development, neuronal migration, cell adhesion, and formation of neuronal circuits [33–35]. Protocadherins alpha, beta, and gamma, are encoded in a single cluster in mammalian genomes, which undergo stochastic regulation of expression and alternative splicing, producing complex ensembles of gene and isoform combinations. This combinatorial expression, conserved within cell lineages, generates address codes required for neuronal identity, and self/non-self-discrimination. Single nucleotide polymorphisms in the protocadherin locus have been linked to neurodevelopmental disorders including autism and schizophrenia [34]. Dysregulation of protocadherin expression suggests aberration in neuronal circuit assembly and altered development of cell lineages.

Monocyte to macrophage differentiation-associated (*Mmd*, Figure 9f), which encodes the PAQR11 protein, is predicted to be involved in positive neuron differentiation. It is a Golgi scaffold protein [36] participating in lipid metabolism [37], and a marker of macrophage differentiation [38]. It is broadly expressed in the brain, but its function in neurons is currently unknown.

Wac haploinsufficiency has been linked to immune dysfunction and hypogammaglobulinemia [2]. Dysregulation of genes involved in cytokine production (*Bcl6*, *Adam33*, and *Pdeb4*) provides further context to this report (Figure 9e, 9g). *Adam33* encodes a scaffold protein regulating cytokine secretion, mostly known as an asthma susceptibility gene [39]. Phosphodiesterase 4B (*Pde4b*), encodes an enzyme hydrolyzing second messenger cAMP, which is a risk gene for psychiatric illness including schizophrenia and bipolar disorder, and a target of antidepressant therapies [40]. The family of phosphodiesterase genes has been implicated in autism [41], and a hypomorphic mutant of *Pde4b* exhibited more neurogenesis and behavioral deficits [42].

RNF20/40/WAC complex plays an important role in regulating chromatin accessibility and transcription through H2B ubiquitination [7]. It also mediates transcription elongation, and indirectly, splicing [43]. We performed event-based differential splicing (DS) analysis using MAJIQ2.5 pipeline [44]. We found 13 DS junctions passing thresholds of 10% delta percent spliced in (dPSI) between WT and *Wac* Het, at 80% confidence level. As expected, we found two significant events representing floxed *Wac* exon skipping, and one intron retention in the *Cre* transgene locus *Gt(ROSA)26Sor*. We also detected skipped exons in *Snhg14*, alternative splice donors in *Dnmbp* and *Trmt61b*, alternative splicing acceptors in *Ssrp1* and *Trmt13*, retained introns in *Gm21992* and *Pigf*, and reduced intron retention in *Zc3h7a* (Supplementary Figure 15a, 15b, Supplementary Table 7). None of these genes were identified as significantly differentially expressed. Alternative splicing of *Snhg14*, is of particular interest. It is an antisense transcript located in the *Ube3a* locus, a genomic region orthologous to human 15q11-13, which loss of function and imbalanced imprinting is responsible for neurodevelopmental disorders Prader-Willi and Angelman syndromes. Differential splicing of *Ssrp1*, which encodes a protein member of the chromatin transcription elongation complex FACT, suggests presence of a feedback mechanism regulating transcription elongation [45]. Overall, our data shed new light on the transcriptomic mechanisms and phenotypes of *Wac* haploinsufficiency and provide further context for the existing studies of DESSH syndrome.

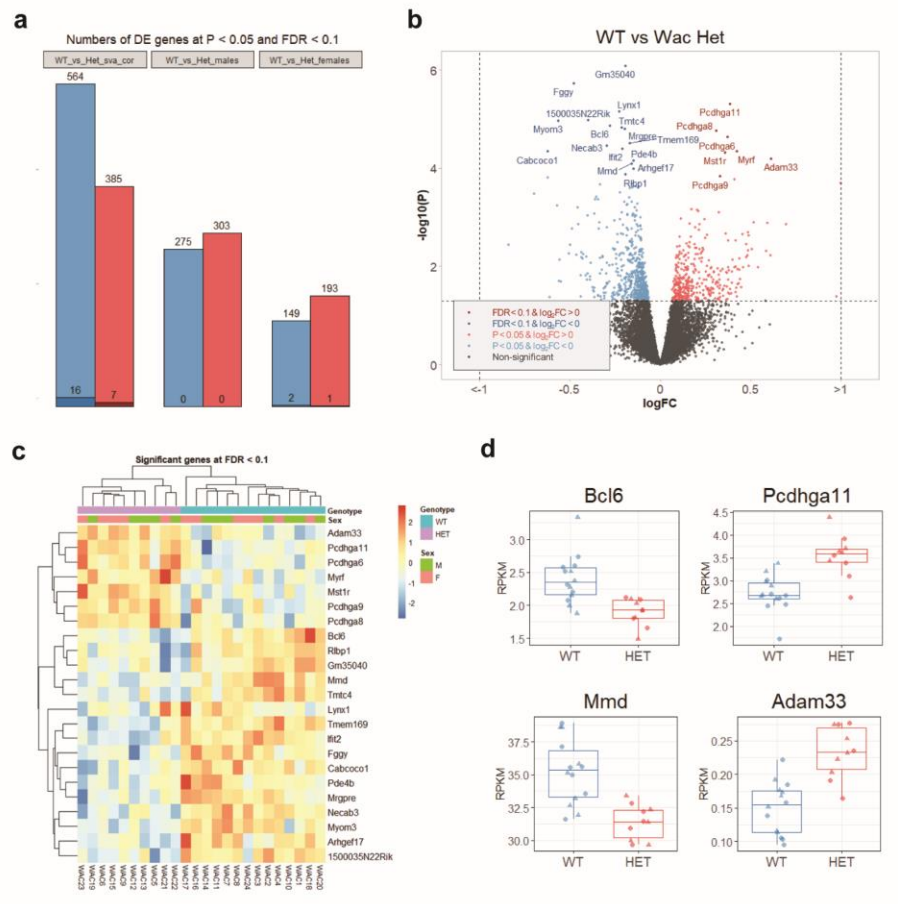

Figure 9. Transcriptomic characterization by bulk RNA-seq. (a) Numbers of upregulated and downregulated, red and blue, respectively, differentially expressed (DE) genes. Lighter colors represent P < 0.05 and darker colors represent FDR < 0.1 thresholds. Three DE groups represent 1) SVA-corrected DE model combining samples from both sexes. 2) Male samples, 3) Female samples. (b) Volcano plot representing DE of the SVA-corrected DE model in (a). Labeled genes pass FDR < 0.1. (c) Heatmap representing RPKM expression of 23 DE genes passing FDR < 0.1. Colors represent $\log_2$-transformed RPKM values, Z-scaled across samples. (d) Gene ontology (GO) biological process enrichment analysis of 23 genes passing FDR < 0.1. Annotated - number of genes in a GO term; Significant - number of genes passing FDR < 0.1; Expected - number of genes in a GO term expected at random; classicFisher – Fisher exact test P value; Enrichment – $\log_2$ ratio of Significant + 1 to Expected + 1, representing GO term enrichment effect size. (efgh) Box plots of RPKM expression values of significantly DE genes belonging to enriched GO terms in (d). Triangles represent female, circles represent male samples.

Discussion

DESSH syndrome is a monogenic syndrome that results in variable degree of developmental delay/intellectual disability, craniofacial dysmorphic features, ophthalmological and gastrointestinal problems, hypotonia, epilepsy and other neurological changes that may underlie the elevated co-diagnoses of ASD and ADHD. Previous work implied that dysfunction of the *Wac* gene is associated with DESSH syndrome symptoms, thus we sought to test if genetic depletion of the *Wac* gene could recapitulate some of the reported symptoms in distinct vertebrate models. To this end, we depleted *Wac* in both mouse and zebrafish models and assessed their unique advantages and overlapping phenotypes. Overall, these data provide evidence that each model indeed shows

evidence of relevant phenotypes to individuals diagnosed with DESSH and could prove to be great tools in understanding the biological mechanisms underlying the syndrome as well as testing future therapeutics.

Dysmorphic facial features are observed in DESSH syndrome [1]. To this end, we found a broadening of the fontanels and sutures along the midline of the calvaria in mice; this was maintained in anterior regions at adult stages. Since zebrafish have two copies of the *wac* gene, *waca* and *wacb*, each was initially assessed for phenotypes but only loss of *waca* generated any phenotypes thus far. This is important to understand as duplication of a gene may allow one to have divergent functions as the animal evolves. We were able to generate *waca wacb* double KOs with more severe phenotypes but only in small numbers that survived, suggesting that *wacb* may have some compensatory functions to *waca.* However, loss of *wacb* alone was not sufficient to cause any DESSH relevant phenotypes. With regards to craniofacial changes, zebrafish *waca* mutants exhibited similar disturbances to mice, suggesting that craniofacial development is impacted in both vertebrate models. This is important because individuals with DESSH syndrome exhibit similar features, including a broad forehead and hypertelorism, suggesting these models can recapitulate some craniofacial features relevant to DESSH syndrome.

Behavior difficulties are also very common in DESSH syndrome. Both vertebrate models demonstrated deficits in social paradigms and cognition. Uniquely, mice showed deficits in a working memory task while zebrafish mutants were hyperactive; each of these findings may benefit future studies as more behaviors are documented and cognitive abilities studied in patients and animal models.

We also investigated anatomical, cellular and molecular changes in each model. Importantly, mutant male mice have volumetric increases in several brain regions in adult, suggesting sex differences may arise in DESSH patients as they age. Gross brain cell types were not grossly impacted. However, both mutants had deficits in GABAergic markers. Mutant zebrafish showed a gross change in a general GABAergic marker in the forebrain area while mice had decreased GABAergic subtype marker, PV. This is important because it implicates GABAergic development as a potential target for future studies and therapeutics. These changes may also be important for behavioral changes relevant to DESSH. We and others have observed subtle decreases of PV expression in other syndromic mouse models, including *Cntnap2* [22, 46, 47], suggesting this may be a common feature in some monogenic syndromes with overlapping phenotypic features.

Our transcriptomic characterization of the *Wac* mouse model at P2 identified DE genes enriched in cell adhesion, neuron differentiation and cytokine production. The magnitude of DE was stronger in males and highly concordant in females. DS analysis identified 13 altered splicing events in 9 genes, including *snhg14*, an antisense transcript in the *Ube3a* locus, associated with Angelman and Prader-Willi syndromes, suggesting convergence of neurodevelopmental pathways. To determine which cell types are affected by *Wac* haploinsufficiency our DE and DS results need further validation at the single cell level. Overall, our transcriptomic results support a role for *Wac* in neurodevelopment and regulation of transcription.

Finally, a subset of individuals with DESSH syndrome have seizures [1, 3, 4, 15]. We found that subthreshold GABAA receptor inhibition elicited seizures in *Wac* Het mice. The reaction to PTZ suggest that their brains are shifted towards increased excitability. It is also possible that this more excitable brain may influence the expression of PV, as we and others have found that brain activity can alter PV expression [24, 48]. Thus, it is still unclear whether the loss of PV leads to seizures in our model or if the elevated brain excitability could lead to changes in PV expression. No matter the cause, others have noted the importance of PV expression on behaviors relevant to ASD [49], suggesting that approaches to target PV expressing neurons may be a future therapeutic to alleviate some symptoms of DESSH syndrome. We validated new vertebrate models with features relevant to DESSH syndrome. These phenotypes are a first attempt to understanding this complex rare disorder and offer tools to probe further biological mechanisms and therapeutics.

Materials and methods

Animals: ***Mouse model.*** We thank the Wellcome Trust Sanger Institute Mouse Genetics Project (Sanger MGP) and its funders for providing the conditional mutant mouse gamete (C57BL/6N-Wac<tm2c(EUCOMM)Wtsi>/Wtsi). Funding information may be found at www.sanger.ac.uk/mouseportal, associated primary phenotypic information at www.mousephenotype.org and data about the development of these technologies [50–54]. Data specifically related to *Wac* can be accessed here

https://www.mousephenotype.org/data/genes/MGI:2387357. Sperm harboring the *Wac* conditional allele was used to fertilize C57BL6/N donor eggs; progeny were then genotyped via polymerase chain reaction (PCR). We next bred *Beta actin-Cre* mice [12] with Wac^{Flox} mice to generate wild type (WT) and constitutive Het mice. After germline recombination, *Wac* Het mice were backcrossed and bred with CD-1 mice for at least three generations before being used for experiments, which were performed under the approval of Michigan State University's Campus Animal Resources. For all experiments, littermate WT controls were compared to *Wac* Hets. ***Zebrafish model.*** Zebrafish (*Danio rerio*) were maintained at 28.5℃ with a 14 hours light/10 hours dark condition and fed three times a day. Zebrafish embryos were cultured in egg water (pH 7.4) and embryonic stages were determined by standard method [55]. All zebrafish experiments were approved by the Institutional Animal Care and Use Committees (IACUC) of Chungnam National University (CNU-00866) and zebrafish reared by standard lab protocols.

Generation of *waca/wacb* KO zebrafish: Zebrafish *waca* and *wacb* gene sequences were acquired from the NCBI database (*waca*: NM_199660.1, *wacb*: NM_001005971.1). Primers for in vitro transcription of sgRNAs were designed by 5′- TAATACGACTCACTATAGCTACTACAACTGCAGGACAGGTTTTAGAGCTAGAA -3′ and 5′- TAATACGACTCACTATAGAGACAAGCATAGTGACGGGAGTTTTAGAGCTAGAA -3' for *waca* and *wacb* target sites, respectively. Primers contained 5' T7 promoter and 15 nucleotides at 3' complement to the universal primer. Templates for *in vitro* transcription of sgRNAs to knock-out *waca* or *wacb* targets were produced by PCR with universal primer 5' – TAATACGACTCACTATAGGGAGGAAGGACTGGCACACGTTTTAGAGCTAGAA – 3' [56]. *In vitro* transcription was carried out using PCR products and MaxiScript T7 Kit (Ambion). Cas9 expression vector pT3TS-nCas9n (Addgene), linearized with XbaI (NEB) and purified via DNA extraction kit (ELPIS). Cas9 mRNA was synthesized using mMESSAGE mMACHINE T3 Kit (Ambion) and tailed poly (A) with E. coli Poly (A) Polymerase (NEB). sgRNAs of *waca* or *wacb* were injected with Cas9 mRNAs into 1-cell stage embryos.

Behavior (mouse): 6-8 week aged mice of both sexes were tested; no differences were observed in any assay between sexes and data represent both groups. The persons performing the behaviors and analyses were blinded to the genotypes.

3-chamber social interaction: During habituation, test mice had 10 minutes in the center of a rectangular chamber divided into 3-chambers by plexiglass containing small holes to navigate. Side chambers contained empty holders, with small holes allowing snout contact. Following initial habituation, an unfamiliar sex- and age-matched mouse (habituated to round holders/cages previously) was put in one of the chambers randomly with doors of the lateral chambers closed and a novel object in the other. The test subject explored the apparatus for 10 minutes. Sniffing time was recorded using an overhead video camera and analyzed using ANY-Maze software. Time spent in each chamber and interaction with mouse/object was recorded.

Y-maze: Individual mice were placed at the end of one arm of a Y-maze and allowed to explore for five minutes while being filmed by an overhead camera. Entries into all arms were noted (four paws need to be inside the arm for a valid entry) and a spontaneous alternation is counted if an animal enters three different arms consecutively. % of spontaneous alternation were calculated according to following formula: [(number of alternations) / (total number of arm entries − 2)] × 100.

Behavior (zebrafish):
Novel tank assay: Novel tank assay was performed as previously described [57–59]. 3 month/older WT and *waca* KO sibling zebrafish were tested in the behavior tank (24 x 15 x 15 cm). The back and sides were covered with non-transparent white paper. Behavior tests were recorded for 20 minutes using a video camera (Sony, HDRCX190). All fish were returned to facility system tanks after completion of the behavioral tests. Recorded video files were analyzed using EthoVision XT7 software (Noldus).

Social cohesion test: Zebrafish group social cohesion was measured [57, 58]. During one session, 5 WT sibling or *waca* KO sibling zebrafish were placed in the behavior tank. Fish groups were recorded for 20 minutes using a video camera (Sony, HDRCX190). Videos were analyzed using 12 individual screenshots taken every 10 seconds for 3-5 minutes as early phase and 17-19 minutes as late phase. Distances between individual zebrafishes in the group were measured using ImageJ for each screenshot and compiled.

Cranio-facial analyses: ***Mouse model***. The skulls were stained with Alizarin red for bone as previously published [60]. Quantification of the suture and fontanel areas and the skull width was performed from photographs using ImageJ. ***Zebrafish model.*** Zebrafish cartilage was stained by Alcian Blue (Sigma) as previously described [61, 62]. Zebrafish larvae at 13dpf were fixed with 4% paraformaldehyde (PFA) overnight at 4ºC and treated with bleaching solution (3% H_2O_2/0.5% KOH in distilled water) for 30 minutes, rinsed out with Phosphate buffered saline with 0.1% Tween 20 (PBST). Specimens were transferred to methanol to store at -20º. Zebrafish cartilage was stained by Alcian blue solution (0.1% Alcian blue with 70% EtOH) for 1 hour and then dehydrated in 70% EtOH. Specimens were rinsed 100% PBST and then transferred to 90% glycerol with 1% KOH to analyze on a dissecting microscope.

Genotyping: ***Mouse model.*** Primers to detect the recombined allele of the *Wac* genetic locus: Forward 5'-AGCTATGCGTGCTGTTGGG-3' and Reverse 5'-CAAATCCCACAGTCCAATGC-3'. Thermocycling conditions were: 95ºC 3 minutes, (95ºC 30 seconds, 58ºC 30 seconds, and 72ºC 45 seconds for 35 cycles), 72ºC 3 minutes. Sanger sequencing to validate the recombined locus was performed by GeneWiz using the same primers on gel-purified PCR products. ***Zebrafish model.*** Primers to detect the alleles of *waca*: Forward 5'-ATTTGAACCGGCAGATGATT-3' and Reverse 5'-TCAGTGGGAGAAACCCAAAG-3'. Thermocycling conditions were: 95ºC 5 minutes, (95ºC 30 seconds, 60ºC 40 seconds, and 72ºC 20 seconds for 40 cycles), 72ºC 7 minutes and 15ºC 10 minutes. Primers to detect the genotypic alleles of *wacb*: Forward 5'-ATACCAGTCAAAGAGTCACTCAGCGAATGA-3' and Reverse 5'-CACGTTCACCGGCCCCGTGAGAGAGACCAC-3'.

Immuno-fluorescent staining: At P30, mice were transcardially perfused with phosphate-buffered saline (PBS), followed by 4% paraformaldehyde. The brains were then removed and postfixed in PFA for 30 minutes. Brains were transferred to 30% sucrose for cryoprotection overnight after fixation and then embedded in optimal cutting temperature compound before coronally sectioned at 25µm via cryostat. Sections were permeabilized in a wash of PBS with 0.3% Triton-X100, then blocked with the same solution containing 5% bovine serum albumin. Primary antibodies (details can be found in Supplementary Table 8) were applied overnight at 4ºC, followed by 3 washes. Secondary antibodies (Alexa-conjugated 488 or 594 anti-rabbit or mouse, 1:300, Thermo-Fisher) were applied for 1-2 hours at room temperature, followed by 3 washes and cover slipped with Vectashield. Cell counts were performed using Image-J software from images that included all cortical layers.

MRI acquisition and analysis: High-resolution ex vivo MRI was conducted on 4% paraformaldehyde-fixed brains using a 9.4T Bruker Advance (Bruker Biospin, Billerica, MA, USA) with the following parameters: TR/TE 3397/10.6, 10 evenly spaced echoes 10ms apart, matrix 1.75 X 1.25 (91um isotropic), and 30 slices 0.5mm thick. T2-weighted imaging (T2WI) and T2 relaxation maps were computed as we previously described [63]. T2WI scans were skull stripped (masking) using the segmentation tool from the ITK-SNAP software (version 3.8.0, RRID:SCR_002010) [64]. The T2WI mask was then used to generate a 3D reconstruction of the brain. T2WI parametric maps were generated and corrected for bias field inhomogeneities prior to registration. From T2WI data, brain and regional volumes and T2 relaxation times were obtained. The Australian Mouse Brain Mapping Consortium (AMBMC) atlas [65, 66] was utilized to extract 40 bilateral regions using non-linear registration to each subject's T2 images. Regional labels were applied using Advanced Normalization Tools (ANTs) and manually inspected for registration quality. Outliers were identified by calculating the interquartile range (IQR) for each region where 1.5IQR above the first quartile or below the third quartile were identified and excluded using Microsoft Excel.

Microscopy: Mouse fluorescent images were acquired using a Leica DM2000 microscope with a mounted monochrome DFC3000G camera. Fluorescent images were adjusted for brightness/contrast and merged using Image-J software. The skulls were photographed with Nikon SMZ1500 stereomicroscope and Nikon DSRi1 camera. Zebrafish images were acquired using Leica TL 5000 microscope with DFC 7000T camera.

PTZ induced seizure assessments: 1 gram of Pentylenetetrazole (PTZ) powder dissolved into 250 ml of PBS and injected intraperitoneally at 50 mg of PTZ per gram of mouse body weight. After injection, mice explored a clean cage for 20 minutes. Seizure severity was scored based on a modified Racine scale [67]: 1) Freezing or idle behavior; 2) Muscle twitches and/or rhythmic head nodding; 3) Tail arching over the mouse's backside accompanied by the mouse assuming a hunched posture; 4) Forelimb clonus; 5) Tonic-clonic seizures with a recovery to normal behavior; 6) Uncontrolled running/jumping/hyperactivity; 7) Full body extension of limbs; 8) Death.

RNA-Sequencing and bioinformatics analysis: Twenty-four mouse brains (14 WT and 10 *Wac* HETs; 7, 7 and 5, 5, males, females, respectively) were collected at P2 following instant decapitation. Samples were snap frozen on dry ice and stored at -80C until RNA preparation. On the day of RNA isolation, left and right forebrain hemispheres were separated from the hindbrain and the total RNA was consistently isolated from the right forebrain hemisphere. Total RNA was obtained using Ambion RNAqueous Total RNA Isolation Kit (cat# AM1912) and assayed via Agilent RNA 6000 Nano Bioanalyzer kit/instrument. Sample RIN scores ranged from 6.9 to 9.8, with a mean RIN score of 9.4.

Poly-A-enriched mRNA libraries were prepared at Novogene using Illumina reagents. Libraries were sequenced using Illumina NovaSeq 6000 S4 system, paired-end 150 (PE150) method. Reads were aligned to mouse genome (GRCm38/mm10) using STAR (version 2.5.4b) [68], and gene counts were produced using featureCounts (Liao et al., 2014). On average, 50 million paired-end reads (PE) aligned per sample, with a range of 32 to 84 million reads.

Data quality was assessed using FastQC. FastQC: A Quality Control Tool for High Throughput Sequence Data. Available online at: http://www.bioinformatics.babraham.ac.uk/projects/fastqc/ and principal component analysis (PCA) was used to determine presence of sample outliers. All 24 samples were qualified for the analysis. Raw RNA-seq fastq files and a gene count matrix is available on GEO (GSE264597).

Bioinformatic analysis was performed using R programming language version 4.2.1. R: A language and environment for statistical computing. R Foundation for Statistical Computing, Vienna, Austria. URL https://www.R-project.org/ and RStudio integrated development environment version 2023.06.0. RStudio: Integrated Development Environment for R. Posit Software, PBC, Boston, MA. URL http://www.posit.co/. Plots were generated using ggplot2 R package version 3.4.0, URL: https://link.springer.com/book/10.1007/978-3-319-24277-4. Heatmaps were generated using pheatmap R package 1.0.12. pheatmap: Pretty Heatmaps_. R package version 1.0.12, https://CRAN.R-project.org/package=pheatmap. The analysis scripts are available at: https://github.com/NordNeurogenomicsLab/Publications/tree/master/Lee_et.al._2024%2C_Complimentary_vertebrate_*Wac*_models_exhibit_phenotypes_relevant_to_DeSanto-Shinawi_Syndrome.

Differential expression (DE) analysis: For DE analysis we used edgeR R package (Robinson et al., 2010). Genes with a minimum of 1 counts per million (CPM) in at least six samples were included in the analysis. The first surrogate variable from the SVA-batch-correction method was used as a covariate in the edgeR GLM model [69]. For sex-stratified DE, we used a threshold of CPM > 1 in at least 3 samples, and no batch correction. Reads Per Kilobase per Million mapped reads (RPKM) were used for plotting summary heatmaps and expression data of individual genes.

Gene ontology enrichment analysis: To test for enrichment of GO terms we used the TopGO R package version 2.34.0 (Bioconductor). Mouse Gene Ontology (GO) data was downloaded from Bioconductor (org.Mm.eg.db). For the analysis presented here, we restricted our testing to GO Biological Process annotations and required a minimal node size of 20, and at least 2 significantly DE genes in a GO term. We used the internal 'weight01' testing framework and the Fisher exact test, a strategy recommended for gene set analysis that generally accounts for multiple testing comparisons. For GO BP analysis, we reported terms with p-value<0.05. For all enrichment analysis, the test set of DE genes was compared against the background set of genes expressed in our study based on minimum read-count cutoffs described above.

Analysis code is available at:
https://urldefense.com/v3/__https://github.com/NordNeurogenomicsLab/Publications/tree/master/Lee_et.al._2024*2C_Complimentary_vertebrate_Wac_models_exhibit_phenotypes_relevant_to_DeSanto-Shinawi_Syndrome__;JQ!!HXCxUKc!0tNGmjep5OYi3Z-2ICpXdVi5iivlrNqffntUIxCwJDU1JgPyTtFTU7qg0XsXJuzFU4f_7M5FVXwiPayDnAJaasqO$

Western blots: P30 somatosensory cortices were dissected and frozen on dry ice. Next, they were lysed in RIPA buffer containing protease and phosphatase inhibitors and combined with Laemmli buffer containing 2-Mercaptoethanol and incubated at 95ºC for 5 minutes to denature the proteins. Equal amounts of protein lysates were separated on 10% SDS-PAGE gels and then transferred to nitrocellulose membranes. The membranes were washed in Tris-buffered saline with Tween-20 (TBST) and then blocked for 1 hour in TBST containing 5% non-fat dry milk (blotto, sc-2324 SantaCruz biotechnology). Membranes were then incubated with primary

antibodies overnight at 4ºC, washed 3 times with TBST, incubated with secondary antibodies for 1 hour at room temperature and then washed 3 more times with TBST. Membranes were next incubated in ECL solution (BioRad Clarity substrate 1705061) for 5 minutes and chemiluminescent images obtained using a BioRad Chemidoc™ MP imaging system. Primary antibody details can be found in Supplementary Table 8, secondary HRP antibodies were used at 1:4000 (BioRad). Uncropped western blots are shown in Supplementary Figure 16.

Whole-mount *in situ* hybridization (WISH): WISH was performed using DIG-labeled antisense RNA probes for *gad1b*. RNA probes were synthesized using DIG-RNA labeling kit (Roche) [70]. Zebrafish larvae were fixed in 4% PFA in PBS overnight at 4ºC then dehydrated with 100% Methanol. Larvae were rehydrated with 0.1% Diethyl pyrocarbonate with PBST (DEPC-PBST, Sigma Aldrich). Larvae were permeabilized with 10µg/ml proteinase K (Roche) according to developmental stage. Larvae were re-fixed for 15 minutes in 4% PFA, washed with DEPC-treated PBST, and pre-hybridized in HYB solution (50% formamide, 5X saline sodium citrate, 50µ g/ml heparin, 500 µg/ml torula RNA, 46mM citric acid pH 6.0, 0.1% Tween20) for 1 hour at 70ºC. Antisense DIG-labeled RNA probes were added in HYB solution and incubated for overnight at 70ºC. Larvae were washed in a preheated mixture of 50% saline sodium citrate containing 0.1% Tween-20 and 50% hybridization solution at 70ºC. Larvae were blocked and then incubated with 1/4000 concentration of anti-DIG Fab fragment conjugated with alkaline phosphatase (Roche) overnight at 4ºC. Larvae were washed in PBST then incubated in staining solution including NBT/BCIP as alkaline phosphatase substrate in the dark until sufficient staining appeared. Larvae were mounted in 90% glycerol in PBST and were visualized via dissecting microscope.

Quantification and statistical analysis: Statistical analyses were performed using Prism version 7, a p value of < 0.05 was considered significant. For parametric measures of two groups, a two-tailed T-test was performed; parametric measures of three or more groups utilized a ONE-Way ANOVA with Tukey post-test. If different statistical analyses were used they are denoted in figure legends. Supplementary Table 9 has details about statistics employed herein.

Acknowledgements

AMS, **DV**, **KU**, **TEJ** and **XL** were funded by the Michigan State University/Spectrum Health Corporation; we would like to thank DubDub and Harrison Levon-James Allen for critical insights and providing resources during this study; **MP-V** and **JJ** were funded by NIDCR R01 DE026798; **D P-C** was supported by the Integrative Pharmacological Sciences Training Program at Michigan State University, 5T32GM142521-04. **KU**, **TEJ** and **XL** were funded by the Cystic Fibrosis Foundation LI19XX0, the Cystic Fibrosis Research Inc., R01 HL153165-01A1. **ASN** was funded by NIMH R01 MH120513. **C-H K** was supported by grants from the National Research Foundation of Korea (2018M3A9B8021980, 2020R1A5A8017671, and 2021R1A2C1008506). The Neuroscience Program's Discretionary Research Fund at Michigan State University supported the RNA sequencing data presented herein.

Conflict of interests

The authors report that they have no conflict of interests.

References

1. DeSanto C, D'Aco K, Araujo GC, Shannon N, DDD Study, Vernon H, et al. WAC loss-of-function mutations cause a recognisable syndrome characterised by dysmorphic features, developmental delay and hypotonia and recapitulate 10p11.23 microdeletion syndrome. J Med Genet. 2015; 52:754–761.

2. Vanegas S, Ramirez-Montaño D, Candelo E, Shinawi M, Pachajoa H. DeSanto-Shinawi Syndrome: First Case in South America. Mol Syndromol. 2018; 9:154–158.

3. Leonardi E, Bellini M, Aspromonte MC, Polli R, Mercante A, Ciaccio C, et al. A Novel WAC Loss of Function Mutation in an Individual Presenting with Encephalopathy Related to Status Epilepticus during Sleep (ESES). Genes. 2020; 11.

4. Alawadhi A, Morgan AT, Mucha BE, Scheffer IE, Myers KA. Self-limited focal epilepsy and childhood apraxia of speech with WAC pathogenic variants. Eur J Paediatr Neurol. 2021; 30:25–28.

5. Morales JA, Valenzuela I, Cuscó I, Cogné B, Isidor B, Matalon DR, et al. Clinical and molecular characterization of five new individuals with WAC-related intellectual disability: Evidence of pathogenicity for a novel splicing variant. Am J Med Genet A. 2022. https://doi.org/10.1002/ajmg.a.62648.

6. Iossifov I, O'Roak BJ, Sanders SJ, Ronemus M, Krumm N, Levy D, et al. The contribution of de novo coding mutations to autism spectrum disorder. Nature. 2014; 515:216–221.

7. Zhang F, Yu X. WAC, a functional partner of RNF20/40, regulates histone H2B ubiquitination and gene transcription. Mol Cell. 2011; 41:384–397.

8. McKnight NC, Jefferies HBJ, Alemu EA, Saunders RE, Howell M, Johansen T, et al. Genome-wide siRNA screen reveals amino acid starvation-induced autophagy requires SCOC and WAC. EMBO J. 2012; 31:1931–1946.

9. David-Morrison G, Xu Z, Rui Y-N, Charng W-L, Jaiswal M, Yamamoto S, et al. WAC Regulates mTOR Activity by Acting as an Adaptor for the TTT and Pontin/Reptin Complexes. Dev Cell. 2016; 36:139–151.

10. Qi F, Chen Q, Chen H, Yan H, Chen B, Xiang X, et al. WAC Promotes Polo-like Kinase 1 Activation for Timely Mitotic Entry. Cell Rep. 2018; 24:546–556.

11. Rudolph HC, Stafford AM, Hwang H-E, Kim C-H, Prokop JW, Vogt D. Structure-Function of the Human WAC Protein in GABAergic Neurons: Towards an Understanding of Autosomal Dominant DeSanto-Shinawi Syndrome. Biology. 2023; 12:589.

12. Lewandoski M, Meyers EN, Martin GR. Analysis of Fgf8 gene function in vertebrate development. Cold Spring Harb Symp Quant Biol. 1997; 62:159–168.

13. Ho S, Luk H-M, Lo IFM. Extending the phenotype of DeSanto-Shinawi syndrome: A case report and literature review. Am J Med Genet A. 2021. https://doi.org/10.1002/ajmg.a.62571.

14. Uehara T, Ishige T, Hattori S, Yoshihashi H, Funato M, Yamaguchi Y, et al. Three patients with DeSanto-Shinawi syndrome: Further phenotypic delineation. Am J Med Genet A. 2018; 176:1335–1340.

15. Lugtenberg D, Reijnders MRF, Fenckova M, Bijlsma EK, Bernier R, van Bon BWM, et al. De novo loss-of-function mutations in WAC cause a recognizable intellectual disability syndrome and learning deficits in Drosophila. Eur J Hum Genet EJHG. 2016; 24:1145–1153.

16. Hamdan FF, Srour M, Capo-Chichi J-M, Daoud H, Nassif C, Patry L, et al. De novo mutations in moderate or severe intellectual disability. PLoS Genet. 2014;10:e1004772.

17. Alsahlawi Z, Jailani M, Alaradi H, AlAbbad A. A Case of DeSanto-Shinawi Syndrome in Bahrain with a Novel Mutation. Case Rep Pediatr. 2020. 8820966.

18. Kraeuter A-K, Guest PC, Sarnyai Z. The Y-Maze for Assessment of Spatial Working and Reference Memory in Mice. Methods Mol Biol. 2019; 1916:105–111.

19. Lalonde R. The neurobiological basis of spontaneous alternation. Neurosci Biobehav Rev. 2002; 26:91–104.

20. Vogt D, Hunt RF, Mandal S, Sandberg M, Silberberg SN, Nagasawa T, et al. Lhx6 directly regulates Arx and CXCR7 to determine cortical interneuron fate and laminar position. Neuron. 2014; 82:350–364.

21. Vogt D, Cho KKA, Lee AT, Sohal VS, Rubenstein JLR. The parvalbumin/somatostatin ratio is increased in Pten mutant mice and by human PTEN ASD alleles. Cell Rep. 2015; 11:944–956.

22. Vogt D, Cho KKA, Shelton SM, Paul A, Huang ZJ, Sohal VS, et al. Mouse Cntnap2 and Human CNTNAP2 ASD Alleles Cell Autonomously Regulate PV+ Cortical Interneurons. Cereb Cortex. 2018; 28:3868–3879.

23. Kim YJ, Khoshkhoo S, Frankowski JC, Zhu B, Abbasi S, Lee S, et al. Chd2 Is Necessary for Neural Circuit Development and Long-Term Memory. Neuron. 2018; 100:1180-1193.e6.

24. Malik R, Pai EL-L, Rubin AN, Stafford AM, Angara K, Minasi P, et al. Tsc1 represses parvalbumin expression and fast-spiking properties in somatostatin lineage cortical interneurons. Nat Commun. 2019; 10:4994.

25. Angara K, Pai EL-L, Bilinovich SM, Stafford AM, Nguyen JT, Li KX, et al. Nf1 deletion results in depletion of the Lhx6 transcription factor and a specific loss of parvalbumin+ cortical interneurons. Proc Natl Acad Sci. 2020. https://doi.org/10.1073/pnas.1915458117.

26. Wonders CP, Anderson SA. The origin and specification of cortical interneurons. Nat Rev Neurosci. 2006; 7:687–696.

27. Rubin AN, Kessaris N. PROX1: a lineage tracer for cortical interneurons originating in the lateral/caudal ganglionic eminence and preoptic area. PloS One. 2013; 8:e77339.

28. Leek JT, Johnson WE, Parker HS, Jaffe AE, Storey JD. The sva package for removing batch effects and other unwanted variation in high-throughput experiments. Bioinforma. 2012; 28:882–883.

29. Choi J, Crotty S. Bcl6-Mediated Transcriptional Regulation of Follicular Helper T cells (TFH). Trends Immunol. 2021; 42:336–349.

30. Bonnefont J, Tiberi L, van den Ameele J, Potier D, Gaber ZB, Lin X, et al. Cortical Neurogenesis Requires Bcl6-Mediated Transcriptional Repression of Multiple Self-Renewal-Promoting Extrinsic Pathways. Neuron. 2019; 103:1096-1108.e4.

31. Tiberi L, Bonnefont J, van den Ameele J, Le Bon S-D, Herpoel A, Bilheu A, et al. A BCL6/BCOR/SIRT1 complex triggers neurogenesis and suppresses medulloblastoma by repressing Sonic Hedgehog signaling. Cancer Cell. 2014; 26:797–812.

32. Wiegreffe C, Wahl T, Joos NS, Bonnefont J, Liu P, Britsch S. Developmental cell death of cortical projection neurons is controlled by a Bcl11a/Bcl6-dependent pathway. EMBO Rep. 2022; 23:e54104.

33. Wu Q, Jia Z. Wiring the Brain by Clustered Protocadherin Neural Codes. Neurosci Bull. 2021; 37:117–131.

34. Flaherty E, Maniatis T. The role of clustered protocadherins in neurodevelopment and neuropsychiatric diseases. Curr Opin Genet Dev. 2020; 65:144–150.

35. Lefebvre JL. Neuronal territory formation by the atypical cadherins and clustered protocadherins. Semin Cell Dev Biol. 2017; 69:111–121.

36. Tan X, Banerjee P, Guo H-F, Ireland S, Pankova D, Ahn Y-H, et al. Epithelial-to-mesenchymal transition drives a pro-metastatic Golgi compaction process through scaffolding protein PAQR11. J Clin Invest. 2017; 127:117–131.

37. Phadnis VV, Snider J, Varadharajan V, Ramachandiran I, Deik AA, Lai ZW, et al. MMD collaborates with ACSL4 and MBOAT7 to promote polyunsaturated phosphatidylinositol remodeling and susceptibility to ferroptosis. Cell Rep. 2023; 42:113023.

38. Lin Y, Huang M, Wang S, You X, Zhang L, Chen Y. PAQR11 modulates monocyte-to-macrophage differentiation and pathogenesis of rheumatoid arthritis. Immunology. 2021; 163:60–73.

39. Yan F, Hu X, He L, Jiao K, Hao Y, Wang J. ADAM33 Silencing Inhibits Vascular Smooth Muscle Cell Migration and Regulates Cytokine Secretion in Airway Vascular Remodeling via the PI3K/AKT/mTOR Pathway. Can Respir J. 2022. 8437348.

40. Fujita M, Richards EM, Niciu MJ, Ionescu DF, Zoghbi SS, Hong J, et al. cAMP signaling in brain is decreased in unmedicated depressed patients and increased by treatment with a selective serotonin reuptake inhibitor. Mol Psychiatry. 2017; 22:754–759.

41. Delhaye S, Bardoni B. Role of phosphodiesterases in the pathophysiology of neurodevelopmental disorders. Mol Psychiatry. 2021; 26:4570–4582.

42. McGirr A, Lipina TV, Mun H-S, Georgiou J, Al-Amri AH, Ng E, et al. Specific Inhibition of Phosphodiesterase-4B Results in Anxiolysis and Facilitates Memory Acquisition. Neuropsychopharmacol. 2016; 41:1080–1092.

43. Wu C, Cui Y, Liu X, Zhang F, Lu L-Y, Yu X. The RNF20/40 complex regulates p53-dependent gene transcription and mRNA splicing. J Mol Cell Biol. 2020; 12:113–124.

44. Vaquero-Garcia J, Aicher JK, Jewell S, Gazzara MR, Radens CM, Jha A, et al. RNA splicing analysis using heterogeneous and large RNA-seq datasets. Nat Commun. 2023; 14:1230.

45. Wright DE, Wang C-Y, Kao C-F. Flickin' the ubiquitin switch: the role of H2B ubiquitylation in development. Epigenetics. 2011; 6:1165–1175.

46. Peñagarikano O, Abrahams BS, Herman EI, Winden KD, Gdalyahu A, Dong H, et al. Absence of CNTNAP2 leads to epilepsy, neuronal migration abnormalities, and core autism-related deficits. Cell. 2011; 147:235–246.

47. Paterno R, Marafiga JR, Ramsay H, Li T, Salvati KA, Baraban SC. Hippocampal gamma and sharp-wave ripple oscillations are altered in a Cntnap2 mouse model of autism spectrum disorder. Cell Rep. 2021; 37:109970.

48. Patz S, Grabert J, Gorba T, Wirth MJ, Wahle P. Parvalbumin expression in visual cortical interneurons depends on neuronal activity and TrkB ligands during an Early period of postnatal development. Cereb Cortex. 2004; 14:342–351.

49. Wöhr M, Orduz D, Gregory P, Moreno H, Khan U, Vörckel KJ, et al. Lack of parvalbumin in mice leads to behavioral deficits relevant to all human autism core symptoms and related neural morphofunctional abnormalities. Transl Psychiatry. 2015; 5:e525.

50. Pettitt SJ, Liang Q, Rairdan XY, Moran JL, Prosser HM, Beier DR, et al. Agouti C57BL/6N embryonic stem cells for mouse genetic resources. Nat Methods. 2009; 6:493–495.

51. Skarnes WC, Rosen B, West AP, Koutsourakis M, Bushell W, Iyer V, et al. A conditional knockout resource for the genome-wide study of mouse gene function. Nature. 2011; 474:337–342.

52. Bradley A, Anastassiadis K, Ayadi A, Battey JF, Bell C, Birling M-C, et al. The mammalian gene function resource: the International Knockout Mouse Consortium. Mamm Genome. 2012; 23:580–586.

53. Ryder E, Gleeson D, Sethi D, Vyas S, Miklejewska E, Dalvi P, et al. Molecular characterization of mutant mouse strains generated from the EUCOMM/KOMP-CSD ES cell resource. Mamm Genome. 2013; 24:286–294.

54. White JK, Gerdin A-K, Karp NA, Ryder E, Buljan M, Bussell JN, et al. Genome-wide generation and systematic phenotyping of knockout mice reveals new roles for many genes. Cell. 2013; 154:452–464.

55. Kimmel CB, Ballard WW, Kimmel SR, Ullmann B, Schilling TF. Stages of embryonic development of the zebrafish. Dev Dyn. 1995; 203:253–310.

56. Jinek M, Chylinski K, Fonfara I, Hauer M, Doudna JA, Charpentier E. A programmable dual-RNA-guided DNA endonuclease in adaptive bacterial immunity. Science. 2012; 337:816–821.

57. Kim O-H, Cho H-J, Han E, Hong TI, Ariyasiri K, Choi J-H, et al. Zebrafish knockout of Down syndrome gene, DYRK1A, shows social impairments relevant to autism. Mol Autism. 2017; 8:50.

58. Choi J-H, Jeong Y-M, Kim S, Lee B, Ariyasiri K, Kim H-T, et al. Targeted knockout of a chemokine-like gene increases anxiety and fear responses. Proc Natl Acad Sci. 2018; 115:E1041–E1050.

59. Park J-S, Choi T-I, Kim O-H, Hong TI, Kim W-K, Lee W-J, et al. Targeted knockout of duox causes defects in zebrafish growth, thyroid development, and social interaction. J Genet Genomics Yi Chuan Xue Bao. 2019; 46:101–104.

60. Yen H-Y, Ting M-C, Maxson RE. Jagged1 functions downstream of Twist1 in the specification of the coronal suture and the formation of a boundary between osteogenic and non-osteogenic cells. Dev Biol. 2010; 347:258–270.

61. Pruvot B, Curé Y, Djiotsa J, Voncken A, Muller M. Developmental defects in zebrafish for classification of EGF pathway inhibitors. Toxicol Appl Pharmacol. 2014; 274:339–349.

62. Dalcq J, Pasque V, Ghaye A, Larbuisson A, Motte P, Martial JA, et al. RUNX3, EGR1 and SOX9B form a regulatory cascade required to modulate BMP-signaling during cranial cartilage development in zebrafish. PloS One. 2012; 7:e50140.

63. Jullienne A, Hamer M, Haddad E, Morita A, Gifford P, Hartman R, et al. Acute intranasal osteopontin treatment in male rats following TBI increases the number of activated microglia but does not alter lesion characteristics. J Neurosci Res. 2020; 98:141–154.

64. Yushkevich PA, Piven J, Hazlett HC, Smith RG, Ho S, Gee JC, et al. User-guided 3D active contour segmentation of anatomical structures: significantly improved efficiency and reliability. NeuroImage. 2006; 31:1116–1128.

65. Ullmann JFP, Watson C, Janke AL, Kurniawan ND, Reutens DC. A segmentation protocol and MRI atlas of the C57BL/6J mouse neocortex. NeuroImage. 2013; 78:196–203.

66. Richards K, Watson C, Buckley RF, Kurniawan ND, Yang Z, Keller MD, et al. Segmentation of the mouse hippocampal formation in magnetic resonance images. NeuroImage. 2011; 58:732–740.

67. Vogt DL, Thomas D, Galvan V, Bredesen DE, Lamb BT, Pimplikar SW. Abnormal neuronal networks and seizure susceptibility in mice overexpressing the APP intracellular domain. Neurobiol Aging. 2011; 32:1725–1729.

68. Dobin A, Davis CA, Schlesinger F, Drenkow J, Zaleski C, Jha S, et al. STAR: ultrafast universal RNA-seq aligner. Bioinforma. 2013; 29:15–21.

69. Leek JT. Asymptotic conditional singular value decomposition for high-dimensional genomic data. Biometrics. 2011; 67:344–352.

70. Thisse C, Thisse B. High-resolution in situ hybridization to whole-mount zebrafish embryos. Nat Protoc. 2008; 3:59–69.